Posted on 22 Nov 2022 — The copyright holder is the author/funder. All rights reserved. No reuse without permission. — https://doi.org/10.1002/essoar.10507376.1 — This a preprint and has not been peer reviewed. Data may be preliminary.

Implications of laterally varying scattering properties for subsurface monitoring with coda wave sensitivity kernels: application to volcanic and fault zone setting

Chantal van Dinther[1], Ludovic Margerin[2], and Michel Campillo[3]

[1]ISTerre, UGA
[2]Paul Sabatier University - Toulouse III
[3]Université Joseph Fourier, Grenoble

November 22, 2022

Abstract

Monitoring changes of seismic properties at depth can provide a first order insight into Earth's dynamic evolution. Coda wave interferometry is the primary tool for this purpose. This technique exploits small changes of waveforms in the seismic coda and relates them to temporal variations of attenuation or velocity at depth. While most existing studies assume statistically homogeneous scattering strength in the lithosphere, geological observations suggest that this hypothesis may not be fulfilled in active tectonic or volcanic areas. In a numerical study we explore the impact of a non-uniform distribution of scattering strength on the spatio-temporal sensitivity of coda waves. Based on Monte Carlo simulation of the radiative transfer process, we calculate sensitivity kernels for three different observables, namely travel-time, decorrelation and intensity. Our results demonstrate that laterally varying scattering properties can have a profound impact on the sensitivities of coda waves. Furthermore, we demonstrate that the knowledge of the mean intensity, specific intensity and energy flux, governed by spatial variation of scattering strength, is key to understanding the decorrelation, travel-time and intensity kernels, respectively. A number of previous works on coda wave sensitivity kernels neglect the directivity of energy fluxes by employing formulas extrapolated from the diffusion approximation. In this work, we demonstrate and visually illustrate the importance of the use of specific intensity for the travel-time and scattering kernels, in the context of volcanic and fault zone setting models. Our results let us foresee new applications of coda wave monitoring in environments of high scattering contrast.

Implications of laterally varying scattering properties for subsurface monitoring with coda wave sensitivity kernels: application to volcanic and fault zone setting

Chantal van Dinther [1], Ludovic Margerin [2], Michel Campillo [1]

[1]Université Grenoble Alpes, ISTerre, C.N.R.S., B.P. 53, 38041 Grenoble, France.
[2]Institut de Recherche en Astrophysique et Planétologie, Université Toulouse III Paul Sabatier, C.N.R.S., C.N.E.S, 14, Av. Edouard Belin, 31400 Toulouse, France.

Key Points:

- A non-uniform distribution of scattering strength can have a profound impact on the spatio-temporal sensitivity of coda waves.
- We illustrate this using Monte Carlo simulations for models with either a volcanic, fault zone or two half-spaces setting.
- The mean intensity, specific intensity and energy flux, is key to understanding the decorrelation, travel-time and intensity kernels, respectively.

Corresponding author: Chantal van Dinther, `chantal.van-dinther@univ-grenoble-alpes.fr`

Abstract

Monitoring changes of seismic properties at depth can provide a first order insight into Earth's dynamic evolution. Coda wave interferometry is the primary tool for this purpose. This technique exploits small changes of waveforms in the seismic coda and relates them to temporal variations of attenuation or velocity at depth. While most existing studies assume statistically homogeneous scattering strength in the lithosphere, geological observations suggest that this hypothesis may not be fulfilled in active tectonic or volcanic areas. In a numerical study we explore the impact of a non-uniform distribution of scattering strength on the spatio-temporal sensitivity of coda waves. Based on Monte Carlo simulation of the radiative transfer process, we calculate sensitivity kernels for three different observables, namely travel-time, decorrelation and intensity. Our results demonstrate that laterally varying scattering properties can have a profound impact on the sensitivities of coda waves. Furthermore, we demonstrate that the knowledge of the mean intensity, specific intensity and energy flux, governed by spatial variation of scattering strength, is key to understanding the decorrelation, travel-time and intensity kernels, respectively. A number of previous works on coda wave sensitivity kernels neglect the directivity of energy fluxes by employing formulas extrapolated from the diffusion approximation. In this work, we demonstrate and visually illustrate the importance of the use of specific intensity for the travel-time and scattering kernels, in the context of volcanic and fault zone setting models. Our results let us foresee new applications of coda wave monitoring in environments of high scattering contrast.

Plain Language Summary

To monitor the evolution of the dynamic Earth, seismologists use a part of the seismic record called 'coda', which is composed of waves that have bounced multiple times off heterogeneities of the crust. The coda is extremely sensitive to weak perturbations of propagation properties induced by Earth's tectonic and volcanic activity. The correct physical modeling of coda waves is therefore key to unravel the rich information encoded in their waveforms. A limitation of current seismological monitoring techniques is the neglect of strong lateral variations of coda waves propagation properties documented by geological observations. Our work focuses specifically on this aspect. We provide a complete theoretical and numerical framework to model and understand the spatial and temporal sensitivity of coda waves to medium perturbations in complex geological settings.

Using simple but realistic models of a fault zone and a volcano, we illustrate the profound impact of non-uniform scattering properties on the coda wave sensitivity, which in turn determines the ability of seismologists to correctly retrieve the magnitude and location of physical changes in the crust. Our results let us foresee new applications of coda wave monitoring in environments of high scattering contrast, such as volcanic and fault zone settings.

1 Introduction

With the recent advancements in seismic sensor techniques and the rapid deployment of (dense) seismic arrays over the last decade, there has been a surge in the number of monitoring studies aiming to capture the dynamic evolution of the subsurface. Due to scattering, coda waves sample a large volume of the subsurface densely for long propagation times and are thus sensitive to weak changes of the medium. Consequently, coda waves may be more suitable to characterise temporal variations of the Earth's crust than direct waves, which only sample a narrow volume along the ray path between the (virtual) source and detector. Poupinet et al. (1984) were first to demonstrate the feasibility of monitoring weak changes in apparent velocity caused by fault activity in California using coda waves. Poupinet et al. (1984) derived these global medium changes by measuring the phase shift between the coda of earthquake doublets. In numerical and lab experiments, the extreme sensitivity of the seismic coda to temporal medium changes has also been demonstrated by Snieder et al. (2002). Later, detection of temporal medium changes has been successfully applied using the coda of earthquake records or the coda of ambient noise cross-correlations in numerous settings including but not limited to: volcanoes (e.g. Sens-Schönfelder & Wegler, 2006; Mordret et al., 2010; Brenguier et al., 2016; Hirose et al., 2017; Sánchez-Pastor et al., 2018; Mao et al., 2019; Obermann, Planes, et al., 2013), fault zones (e.g. Schaff & Beroza, 2004; Peng & Ben-Zion, 2006; Wu et al., 2009; Roux & Ben-Zion, 2014; Rivet et al., 2014; Brenguier et al., 2008; Chen et al., 2010), and CO_2 and geothermal reservoirs (Hillers et al., 2020, 2015; Obermann et al., 2015).

Although measurements of temporal medium changes are interesting in their own right, knowledge about their spatial location is necessary to gain more insight into the processes that occur at depth. Regionalization of data can yield a first order estimate on the spatial distribution, but a preferable approach is to perform a (linear) inversion using so-called sensitivity kernels. In loose terms, these spatial weighting functions provide information on the parts of the medium that have preferentially been sampled by the waves in a probabilistic sense. The first travel-time sensitivity kernels for coda wave interferometry have been introduced by Pacheco and Snieder (2005) under the diffusion approximation. Shortly after, Pacheco and Snieder (2006) provided probabilistic kernels for the single scattering regime. Both kernels are in the form of a spatio-temporal convolution of mean intensities of the coda waves. Obermann, Planes, et al. (2013) applied those kernels to invert for structural and temporal velocity changes around the Piton de la Fournaise volcano on Reunion Island. To detect and locate medium changes caused by the M_w 7.9, 2008 earthquake in Wenchuan in China, Obermann et al. (2019) used a 3-D kernel combining the sensitivity of body and surface waves. Although the results of the authors were very promising, Margerin et al. (2016) raised questions about the formulas used to compute the sensitivity kernels, since the works rely on an extrapolation of a formula established in the diffusion regime. Margerin et al. (2016) demonstrated that knowledge of the angular distribution of the energy fluxes of coda waves is required for an accurate prediction of sensitivities, valid for an arbitrary distribution of heterogeneities and all propagation regimes. The authors obtained this result by using a radiative transfer approach, which directly predicts specific intensities. Other developments on sensitivity kernels focus on the sensitivity as a function of depth. Obermann et al. (2016); Obermann, Planès, et al. (2013) showed that a linear combination of the 2-D surface wave and 3-D body wave kernels are a decent proxy to describe the sensitivity as function of lapse-time and depth. A formal approach to couple body and surface waves is provided by Margerin et al. (2019), leading to a specific formulation of kernels (Barajas, 2021).

Most of these studies on sensitivity kernels provide a solution for statistically homogeneous scattering media, although the interest in extending the sensitivity kernels to non-uniform media is growing, which is especially interesting for monitoring volcanic and fault zone settings. Wegler and Lühr (2001) derived attenuation parameters around the Merapi volcano in Indonesia. The authors found a scattering mean free path (ℓ) as low as 100 m for S waves in the frequency band of 4-20 Hz. They also reported that the scattering attenuation is at least one order of magnitude larger than the intrinsic attenuation around Merapi. Later, Yoshimoto et al. (2006) estimated scattering attenuation in the north-eastern part of Honshu in Japan. For this volcanic area the authors analysed the coda of earthquake records and reported a scattering coefficient of 0.01 km^{-1}

for the frequency of 10 Hz. Another study that analysed the coda of seismograms in a volcanic setting in Japan found the scattering mean free path for P and S waves to be as short as 1 km for the 8-16 Hz frequency band (Yamamoto & Sato, 2010). Recently, Hirose et al. (2019) derived a scattering mean free path $\sim$ 2 km at Sakurajima volcano in Japan, which is much smaller than in the surrounding rock. In a recent study on the western part of the North Anatolian Fault Zone (NAFZ) van Dinther et al. (2020) also found a strong contrast in scattering ($\sim$ factor of 15), with $\ell = 10$ km inside the fault zone and ℓ in the order of 150 km outside the fault zone. Gaebler et al. (2019) found similarly small scattering mean free path values along the northern strand of the NAFZ analysing the energy decay of earthquake records with a central frequency of 0.75 Hz.

The first works considering non-uniform media are by Kanu and Snieder (2015a) and Kanu and Snieder (2015b) in which the authors use ensemble averaging of the coda envelopes modelled by employing the diffusion equation to numerically compute the decorrelation sensitivity kernels, which are interpreted as travel-time kernels, to image velocity variations in 2-D acoustic heterogeneous media. Snieder et al. (2019) adjusted the approach to (1) a 2-D elastic case based on the diffusion equation and (2) a 2-D acoustic case based on radiative transfer theory, for media with weak velocity variations. Building on the work of Snieder et al. (2019) and assuming diffusive wave propagation, Duran et al. (2020) developed a numerical approach to derive elastic and acoustic decorrelation sensitivity kernels for 2-D heterogeneous scattering media. Recently, Zhang et al. (2021) modeled sensitivity kernels for elastic body waves in 2-D random heterogeneous scattering media based on radiative transfer theory using a Monte Carlo approach. The authors use a similar probabilistic approach as is used in current study, but a different computation method. Furthermore, the scattering contrasts considered in current study are larger.

In this work we explore the impact of scattering distribution on coda wave sensitivity kernels for the acoustic scalar case. The parametric part of this study (Section 4.2) aids in the understanding of the kernels. Finally, we show examples of sensitivity kernels for realistic settings.

2 Coda-wave Sensitivity Kernels

When monitoring the subsurface, one aims to invert observations to gain information about the perturbation of medium properties. As the name suggests, the sensitivity kernels quantify the spatial and temporal sensitivity of a specific observable to changes in the medium. The kernels facilitate the reconstruction in 2-D or 3-D of the spatial variation of a given physical parameter, such as the wave speed or scattering properties. Since different observations require the use of different kernels, we compute three types of sensitivity kernels: the travel time kernel K_{tt}, the scattering kernel K_{sc} and the decorrelation kernel K_{dc}.

The travel-time kernel, K_{tt}, relates the observed travel-time delay (or phase shifts) between data for different recording periods,which can be seen as apparent velocity changes, to the macroscopic true changes in elastic medium properties. In this study we use the kernel as defined by Margerin et al. (2016); Mayor et al. (2014):

$$K_{tt}\left(\mathbf{r}', t; \mathbf{r}, \mathbf{r}_0\right) = S^D \int_0^t \int_{S^D} \frac{I\left(\mathbf{r}', t-t', -\mathbf{n}'; \mathbf{r}\right) I\left(\mathbf{r}', t', \mathbf{n}'; \mathbf{r}_0\right) dt' dn'}{I\left(\mathbf{r}, t; \mathbf{r}_0\right)} \tag{1}$$

where S^D denotes the unit sphere in space dimension D, as well as its area. The intensity propagators I, for the intensities traveling from a source of forward intensity ($\mathbf{r}$; in applications this can be seen as the 'source') to a source of backward intensity ($\mathbf{r}_0$; 'detector'), via a perturbation ($\mathbf{r}'$), are based on the 2-D radiative transfer equation (RTE; Sato (1993); Paasschens (1997)). I will be presented in greater details later in this manuscript (see Section 4.1 for the description of the source of forward and backward intensity).

Note that the intensity, or energy density, has dimension $[L]^{-D}$ (Paasschens, 1997) so that the kernel has dimension $[t][L]^{-D}$. The kernels are a time density, such that they are equal to the time spent by the waves around a given point, per unit volume or surface. The numerator of Eq. (1) is a convolution between *specific* intensities of two sources, one source of forward intensity and one of backward intensity. A specific intensity is defined as the amount of energy flowing around direction $\mathbf{n}'$, through a small surface element dS located at point $\mathbf{r}$ and at a certain time t within a defined frequency band (e.g. Margerin, 2005). The validity of the kernels also holds for anisotropic scattering, although we consider only isotropic scattering in current work. Previously, Mayor et al. (2014) introduced a sensitivity kernel for the perturbation of intensity caused by a local change in absorption. In Margerin et al. (2016) this sensitivity kernel is reinterpreted probabilistically as the travel-time kernel.

A structural change in the subsurface, e.g. the growth of a fault, results in a perturbation of scattering. An extra scatterer creates new propagation paths for the waves, which in turn slightly modifies the coda signal. As a consequence, one can observe a decorrelation of the waveform in the recordings for different periods of time (Planès et al., 2014). The decorrelation kernel, K_{dc}, relates this observation to the change in scattering of the medium. The kernel takes into account the new propagation paths that have been created by the addition of scatterers, and is defined as follows (Planès et al., 2014; Margerin et al., 2016):

$$K_{dc}\left(\mathbf{r}', t; \mathbf{r}, \mathbf{r}_0\right) = \int_0^t \frac{I\left(\mathbf{r}', t-t'; \mathbf{r}\right) I\left(\mathbf{r}, t'; \mathbf{r}_0\right) dt'}{I\left(\mathbf{r}, t; \mathbf{r}_0\right)} \tag{2}$$

The intensities in Eq. (2) are *mean* intensities, therefore the decorrelation kernel is dependent on the mean energy densities only and not on the directivity of the intensities. Note that formula (2) is valid stricto sensu in the case where the structural change behaves as isotropic scatterers. In the scalar approximation employed in this work, this implies that they are small compared to the probing wavelength. We emphasize that the scattering properties of the reference medium may be completely arbitrary. Another observation for the same medium change, i.e. the scattering perturbation, is a change in intensity δI. Since the observation is different than in the case of the decorrelation, one needs another sensitivity kernel. Physically, a perturbation in scattering located in a volume $\mathrm{d}V(\mathbf{r}')$ has two effects on the intensity. (1) An energy loss, which can be quantified by evaluating the extra-attenuation of seismic phonons that cross $\mathrm{d}V(\mathbf{r}')$. This is effectively what can be monitored with K_{tt}. (2) An increased probability of energy reaching the detector due to the additional paths created by the additional scatterer. This is effectively what K_{dc} provides us with. Therefore, the scattering sensitivity kernel K_{sc}, as derived by Mayor et al. (2014), is defined as:

$$K_{sc}\left(\mathbf{r}', t; \mathbf{r}, \mathbf{r}_0\right) = K_{dc}\left(\mathbf{r}', t; \mathbf{r}, \mathbf{r}_0\right) - K_{tt}\left(\mathbf{r}', t; \mathbf{r}, \mathbf{r}_0\right) \tag{3}$$

Note that the scattering pattern of the new scatterers should be isotropic implying as above that they are small compared to the wavelength. A characteristic of this kernel is that the integral over all detection points $\mathbf{r}$ gives 0, implied by the conservation of energy as demonstrated in the work of Mayor et al. (2014). We will also find in the results (e.g. Fig. 2) that the scattering kernels have both positive and negative sensitivities to scattering perturbations. In other words, the spatial distribution of intensities is modified while the total intensities remain unchanged. For an extension of formulas (1), (2) and (3) to coupled P and S waves, the reader is referred to Zhang et al. (2021).

3 Calculation of Sensitivity Kernels: a Monte Carlo Simulation Approach

To compute the above defined sensitivity kernels we perform Monte Carlo simulations based on the 2-D RTE with isotropic scattering. This section is rather technical in nature and may be read independently from the rest of the manuscript. We recall that in a Monte Carlo approach (e.g. Margerin et al., 2000), the transport of energy is represented by random walks of discrete seismic "phonons" (Shearer & Earle, 2004) that undergo a sequence of collisions in a scattering and absorbing medium. In practice, the medium is often discretized onto elementary volumes where the number of phonons is monitored as a function of time to estimate the energy density. But it is also possible to compute the energy density detected at a specific point of the medium by evaluating the probability for the phonon to return to the detector at each scattering event (see e.g. Hoshiba, 1991, for a detailed treatment). In the present work, we adopt the latter approach.

While early applications focused mostly on the computation of energy envelopes, the introduction of sensitivity kernels based on RTE has stimulated the development of Monte Carlo approaches to compute the derivatives of seismogram envelopes with respect to attenuation model parameters. In a recent investigation of PKP precursors, Sens-Schönfelder et al. (2020) use Monte Carlo simulations to compute the forward and backward intensities propagating from the source to the perturbation and from the detector to the perturbation, respectively. The convolution integral in Eq. (2)-(3) is then evaluated numerically. The method highlights very nicely the regions of the deep Earth contributing to the detection of precursors. Recently, Zhang et al. (2021) generalized the radiative transfer formulation of sensitivities to the case of elastic body waves. These authors illustrate numerically the impact of non-uniform attenuation properties on the spatio-temporal dependence of the kernels in 2-D elastic media. The numerical approach is similar to Sens-Schönfelder et al. (2020) that relies on the convolution of forward and backward (specific) intensities evaluated by the Monte Carlo method. In this work, we propose yet another computational approach to the computation of kernels in non-uniform scattering media that exploits the idea of differential Monte Carlo simulations.

Takeuchi (2016) introduced a differential Monte Carlo method where both the envelope and its partial derivative are calculated in a single simulation. An interesting application of the method, highlighting both the lateral and depth dependence of attenuation in Japan, has been provided by Ogiso (2019). In this work, we also employ the differential approach but in a way quite distinct from Takeuchi (2016). For clarity, we recall the basic ingredients of the method in the next section.

3.1 Differential Monte Carlo Approach

The central idea of the differential Monte Carlo method is best explained with an example (see Lux & Koblinger, 1991, for a detailed treatment). Consider for instance the impact of a perturbation of the scattering coefficient on the energy density. Suppose that a seismic phonon has just been scattered at point $\mathbf{r}'$ in a reference medium with scattering coefficient g. The probability density function (pdf) of the position $\mathbf{r}$ of the next collision point may be written as:

$$P(\mathbf{r};\mathbf{r}'|g) = g(\mathbf{r})e^{-\int_{\mathbf{r}'}^{\mathbf{r}} g(\mathbf{x})dx} \tag{4}$$

where the integral is carried on the ray connecting the point $\mathbf{r}'$ to the point $\mathbf{r}$. Note that we allow the scattering coefficient to vary spatially in the reference medium. The distribution of path length in the perturbed medium is obtained by the substitution $g \to g + \delta g$ in Eq. (4). In the differential Monte Carlo method, the envelopes in the reference and perturbed medium are calculated simultaneously via a biasing scheme for the latter (Lux & Koblinger, 1991). To picture the idea, one may imagine a "true" phonon propagating in the reference medium and a "virtual" mate following *exactly* the same trajectory as the "true" phonon albeit in the perturbed medium. As the phonon propagates in the reference medium, the statistical weight of its virtual mate is updated to compensate exactly for the genuine frequency of occurrence of the path in the perturbed medium. As an example, let us consider the change of weight occurring after the phonon has left the collision point $\mathbf{r}'$ until it is scattered again at point $\mathbf{r}$. Denoting by w the correction factor, we find:

$$
\begin{aligned}
w(\mathbf{r};\mathbf{r}') =& \frac{P(\mathbf{r};\mathbf{r}'|g+\delta g)}{P(\mathbf{r};\mathbf{r}'|g)} \\
=& \frac{(g(\mathbf{r})+\delta g(\mathbf{r}))e^{-\int_{\mathbf{r}'}^{\mathbf{r}} \delta g(\mathbf{x})dx}}{g(\mathbf{r})}
\end{aligned}
$$

An obvious condition of applicability is that $g(\mathbf{r}) > 0$, implying that a collision is indeed possible at the point $\mathbf{r}$ in the reference medium. We also remark that there is no assumption on the 'smallness' of δg in the derivation of (5). For the computation of sensitivity kernels, we thus further require $\delta g/g \ll 1$ and perform a Taylor expansion to obtain (Takeuchi, 2016; Ogiso, 2019):

$$
w(\mathbf{r};\mathbf{r}') = 1 + \frac{\delta g(\mathbf{r})}{g(\mathbf{r})} - \int_{\mathbf{r}'}^{\mathbf{r}} \delta g(\mathbf{x})dx \tag{5}
$$

The interpretation of the above formula is as follows: as the virtual phonon propagates between the two collision points $\mathbf{r}'$ and $\mathbf{r}$, its weight decreases progressively following the integral term; at the collision point $\mathbf{r}$, its weight undergoes a positive jump $\delta g(\mathbf{r})/g(\mathbf{r})$. These two contributions may respectively be related to the loss and gain terms in Eq. (3).

There are two difficulties in the practical application of formula (5). The first one becomes apparent when one discretizes the kernel onto a grid of pixels (in 2-D, or voxels in 3-D): the path of the particle inside each pixel has to be carefully monitored to calculate the integral in Eq. (5). Such particle tracking can be at the origin of significant computational overhead. The other difficulty is inherent to the spatial variation of the scattering coefficient. Generating the exact path length distribution for the pdf (4) involves the computation of the line integral of g which may be very time consuming. In what follows, we propose a method that solves both of these issues by transferring all the sensitivity computation to collision points. A strength of the method is that particle tracking is minimal. Furthermore, a completely arbitrary distribution of scattering properties -including discontinuities of the scattering coefficient- may be implemented transparently and in an "exact" fashion. The main drawback of the approach is that the introduction of statistical weights may result in an increase of the variance of the results. For the applications at hand, we did not find this issue to be limiting.

3.2 The Method of Null or Delta Collisions

We begin by recalling a simple and very efficient method to simulate the transport of energy in an arbitrarily scattering and absorbing medium, referred to as the method of null or delta collisions (Lux & Koblinger, 1991). The starting point is the radiative transfer equation:

$$(\partial_t + c\mathbf{k}\cdot\nabla + \tau(\mathbf{r})^{-1} + t_a(\mathbf{r})^{-1})e(t,\mathbf{r},\mathbf{k}) = \tau(\mathbf{r})^{-1}\int p(\mathbf{k},\mathbf{k}')e(t,\mathbf{r},\mathbf{k}')dk' \tag{6}$$

where c, τ, t_a and $p(\mathbf{k},\mathbf{k}')$ refer to the energy velocity, the scattering mean free time, the absorption time and the scattering pattern, respectively. The integral on the right-hand side is carried over all the directions of propagation. We remark that Eq. (6) is equivalent to the following modified transport Eq.:

$$\begin{aligned}(\partial_t + c\mathbf{k}\cdot\nabla + \tau(\mathbf{r})^{-1} + t_a(\mathbf{r})^{-1} + \tau_\delta(\mathbf{r})^{-1})e(t,\mathbf{r},\mathbf{k}) = \\ \tau(\mathbf{r})^{-1}\int p(\mathbf{k},\mathbf{k}')e(t,\mathbf{r},\mathbf{k}')dk' + \tau_\delta(\mathbf{r})^{-1}\int \delta(\mathbf{k},\mathbf{k}')e(t,\mathbf{r},\mathbf{k}')dk'\end{aligned} \tag{7}$$

which features a new scattering process with pattern $\delta(\mathbf{k},\mathbf{k}')$ (the delta function on the unit sphere) and mean free time $\tau_\delta(\mathbf{r})$. This new process is characterized by the property that it leaves the propagation direction unchanged. It is worth emphasizing that such delta-collisions or null-collisions do not modify the statistics of true physical scattering events. Because the scattering coefficient of delta-collisions is entirely arbitrary, we may always adjust it in a way such that $\tau_\delta(\mathbf{r})^{-1} + \tau(\mathbf{r})^{-1} + t_a(\mathbf{r})^{-1} = \tau_e^{-1}$, where the extinction time τ_e is *fixed*. By adding the new scattering process, we have in effect turned a possibly very complicated medium into a much simpler one where the extinction length is constant. This method has been implemented by van Dinther et al. (2020) to model the scattering of seismic waves across the North Anatolian fault zone. The price to be paid is that one has to simulate more scattering events than in the original problem. However, in the perspective of computing sensitivities, this is not necessarily a drawback. Indeed, as shown below, all the contributions to the sensitivity come exclusively from collision points in the modified numerical scheme. Fig. 1 shows a graphical representation of this method.

3.3 Sensitivity Computations

We begin by noting that in the numerical simulations, absorption is treated as a phonon capture event, which puts it on the same footing as a scattering event. Indeed,

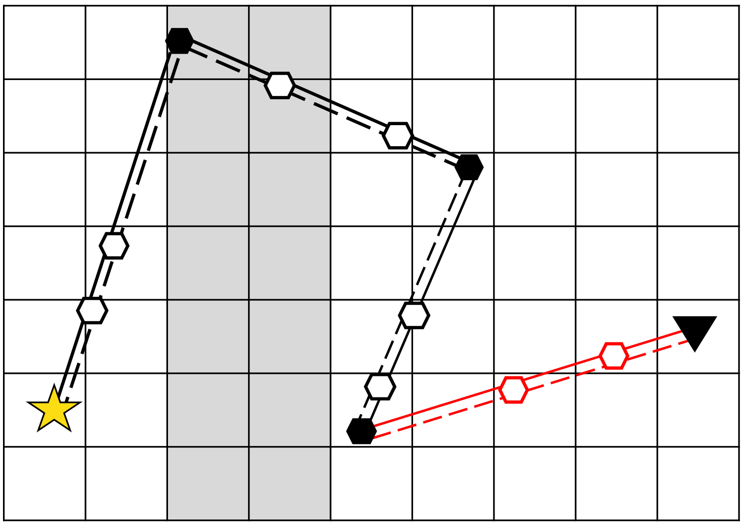

Figure 1. Graphical representation of the flexible Monte Carlo simulation employed in this study. A “true” phonon is propagating through a reference medium from the source (yellow star) to the detector (black triangle). The propagation path of the true phonon is depicted as a solid line. A “virtual” phonon is propagating in a perturbed medium and follows the exact same trajectory, depicted by the dashed line. Between source and detector, the phonons experience delta and physical scattering events (or collisions), indicated by the open and black hexagonals respectively. This implies that we simulate more collisions than there are physical collisions. At every collision we (1) update the weights of the phonons, taking into account the non-uniformity, and (2) compute the sensitivities. The red color highlights the last part of the trajectory toward the detector; in the shown example after three scattering events. The regular grid is indicated by the horizontal and vertical black lines. The simulation can take into account laterally varying scattering properties, represented by the darker pixels. For the simulations this only implies that the phonon weights at the collisions are updated differently.

it is important to keep in mind that the extinction time incorporates the three possible types of interactions: physical scattering, delta scattering and absorption. Rather than terminating the phonon history after an absorption event, we assign a weight w to the particle. At each collision w is multiplied by a factor equal to the local "survival" probability of the phonon $1-t_a(\mathbf{r})^{-1}/\tau_e^{-1}$. That this procedure correctly models the exponential decay of the intensity along its path may be demonstrated heuristically as follows. Consider two neighbouring points on the ray path of a seismic phonon and denote by s a spatial coordinate on the ray. If the path length δs is sufficiently small, we may neglect multiple collision events. In this scenario, either the phonon propagates freely over δs, or it suffers from an additional collision upon which its weight is updated. Hence we have on average:

$$w(s+\delta s) = w(s)\left(1-\frac{\delta s}{c\tau_e}\right) + w(s)\left(1-\frac{t_a(s)^{-1}}{\tau_e^{-1}}\right)\frac{\delta s}{c\tau_e} \tag{8}$$

where we approximate the scattering probability by $(c\tau_e)^{-1}\delta s$. Using a Taylor expansion of the left-hand side, simplifying and rearranging terms we obtain:

$$\frac{dw(s)}{ds} = -\frac{w(s)}{ct_a(s)} \tag{9}$$

which proves the statement. The same line of reasoning will be used below to calculate the contribution of the path from the last scattering event to the detector.

Thanks to these preliminaries, it is now straightforward to apply the differential Monte Carlo method to our problem. As an illustration, let us consider the impact of a scattering perturbation $\delta\tau(\mathbf{r})^{-1}$. Again it is conceptually convenient to consider two phonons: a real phonon propagating in the reference medium and an imaginary phonon propagating in the perturbed medium. We shall also require that the perturbed and unperturbed media have the same extinction time τ_e. Since this parameter can be arbitrarily chosen, this condition can always be fulfilled. By imposing the equality of the extinction time in the reference and perturbed medium, we remove any change of the weight of the virtual phonon in between two collisions. Furthermore, our choice imposes that the rate of delta collisions in the perturbed medium be given by $\tau_\delta^{-1} - \delta\tau(\mathbf{r})^{-1}$. As a consequence, both delta collisions and physical scattering events contribute to the sensitivity to a scattering perturbation. Following the same reasoning as in the derivation of Eq. (5), the weight of the virtual phonon after a delta collision at point $\mathbf{r}$ is updated as follows:

$$\begin{aligned} w(\mathbf{r}) \to & w(\mathbf{r}) \times \frac{\tau_\delta(\mathbf{r})^{-1} - \delta\tau(\mathbf{r})^{-1}}{\tau_e^{-1}} \times \frac{\tau_e^{-1}}{\tau_\delta(\mathbf{r})^{-1}} \\ \to & w(\mathbf{r}) \left(1 - \frac{\delta\tau(\mathbf{r})^{-1}}{\tau_\delta(\mathbf{r})^{-1}}\right) \end{aligned} \tag{10}$$

This last equation highlights that the rate of imaginary collisions must always be strictly positive. The same reasoning applied to a physical scattering event yields:

$$w(\mathbf{r}) \to w(\mathbf{r}) \left(1 + \delta\tau(\mathbf{r})^{-1}/\tau(\mathbf{r})^{-1}\right) \tag{11}$$

Comparing Eq. (5) with Eq. (10)-(11), it is clear that what our method does in effect is to calculate the line integral in (5) by a Monte Carlo approach, where the imaginary collisions serve as sample points for the quadrature. It is however worth noting that we did not make any smallness assumption in the derivation of Eq. (10)-(11). The case of a perturbation of absorption may be treated exactly along the same lines. We find that at imaginary collisions, Eq. (10) applies with the substitution $\delta\tau(\mathbf{r})^{-1} \to \delta t_a(\mathbf{r})^{-1}$.

The last point to be discussed concerns the treatment of the return probability of the phonon from the last scattering event at $\mathbf{r}$ to the detector at $\mathbf{d}$ in the method of partial summations of Hoshiba (1991). The score (or contribution) of the phonon involves the factor $e^{-\int_{\mathbf{r}}^{\mathbf{d}}(t_a(\mathbf{x})^{-1}+\tau(\mathbf{x})^{-1})c^{-1}dx}$ which represents the probability for the phonon to propagate from $\mathbf{r}$ to $\mathbf{d}$ (or beyond) without absorption or physical collisions. It is clear that any perturbation of attenuation properties affect the line integral. We could of course compute this contribution by computing numerically the integral but we would then lose the benefits of the transfer of the sensitivity to collision points. To remedy the difficulty, we replace the numerical quadrature by the following Monte-Carlo procedure:

1. Starting from position $\mathbf{r}$, randomly select the distance L to a new collision point on the ray connecting the last scattering point to the detector. Recall that the pdf of L is simply given by $(\tau_e c)^{-1}\exp(-(\tau_e c)^{-1}L)$.
2. At the collision point, modify the weight of the phonon by the factor $\tau_\delta(r)^{-1}/\tau_e^{-1}$.
3. Compute the factors affecting the sensitivities to scattering (or absorption) following Eq. (10).
4. Repeat (1) until the phonon has traveled beyond $\mathbf{d}$

Steps (1)-(2) simulate the propagation of the phonon from $\mathbf{r}$ to $\mathbf{d}$ in a way such that only delta collisions can occur. The process is enforced by decreasing the weight of the particle by the factor $\tau_\delta(r)^{-1}/\tau_e^{-1}$ at each collision. That the weight of the particle decreases on average as desired can be easily established by following the same heuristic argument as in the derivation of Eq. (8). In step (3), we assume again that the total attenuation is the same in the reference and perturbed medium. Eq. (10) is therefore directly applicable to the computation of the sensitvity to scattering (or absorption) perturbation on the path connecting $\mathbf{r}$ to $\mathbf{d}$.

In numerical applications, the kernels are discretized onto pixels whose dimensions fix the lower bound for the spatial resolution that may be achieved in an inversion. As a consequence, the discretized kernels introduce both spatial and temporal averaging as compared to their analytical counterparts (Mayor et al., 2014). A positive consequence is that all singularities are automatically regularized, which allows for a more straightforward application of the kernels. Furthermore, whereas analytical kernels are attached to the uniform reference medium, the Monte-Carlo approach lends itself naturally to an iterative linearized inversion procedure. From a numerical perspective, the most important feature of our method is the high degree of flexibility, which allows one to very simply model arbitrary non-uniform scattering and absorbing medium, including the presence of discontinuities in the model parameters. We believe that this simplicity largely balances the slowdown entailed by the simulation of artificial scattering events.

For the simulations shown in this manuscript we use a grid of 76-by-76 pixels, where each of the pixels has a dimension of 4-by-4 km. The kernel is evaluated every second, up to a maximum lapse-time of 120 s. The final temporal resolution, however, is 5 s, due to the application of a 5 s moving window to average the kernels and reduce the statistical fluctuations. The total number of phonons simulated for each model is 4×10^9. The distance between the sources, R, equals 32 km for most models (uniform and half-space case), with the placement of the sources at the center of the pixels. For all simulations the full grid space has a uniform value for the intrinsic quality factor $Q_i^{uni} = 100$, based on values recently derived for a normal crustal setting in Turkey, in the vicinity of the Izmit rupture zone (e.g. van Dinther et al., 2020). The scattering mean free path varies depending on the model.

4 Sensitivity Kernels for Non-uniform Scattering Media

In this section we discuss the effect of the scattering distribution on the sensitivity kernels. Guided by the results obtained in a volcanic setting, we introduce the phys-

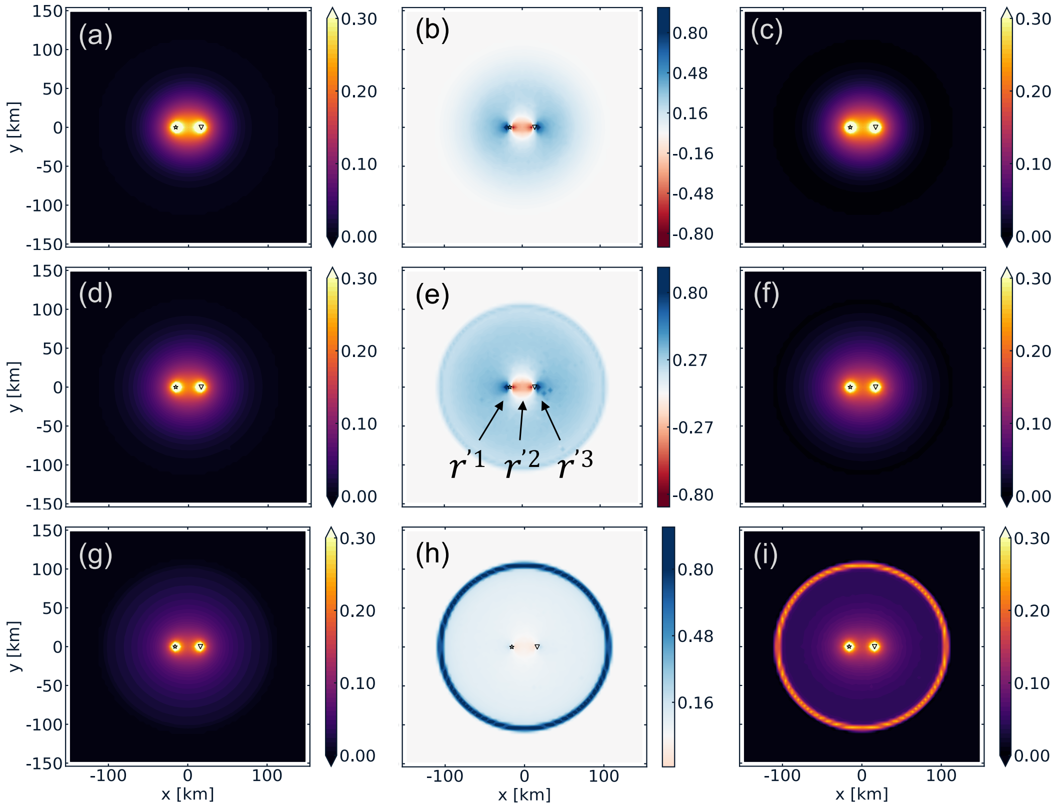

Figure 2. Sensitivity kernels for uniform scattering media at 100 s lapse-time. The columns show K_{tt}, K_{sc} and K_{dc}, respectively. The scattering mean free path increases from top to bottom: ℓ_1, $2{\times}\ell_1$, $8{\times}\ell_1$, with $\ell_1 = 30$ km. The inter-source distance, $R_0 = 32$ km. The annotations r'^1- r'^3 point to positive, negative and positive sensitivity along the line connecting the sources, respectively. All kernels are normalised with respect to the maximum value. Note that for K_{sc} to color bar is symmetric around zero, with red as negative and blue as positive sensitivities, respectively.

ical interpretation for each of the three different kernels. The second context for which we investigate the implications of non-uniform scattering strength on the sensitivities is for a model with two half-spaces. This case is illustrated with the aid of two parametric studies, which facilitate the interpretation of the kernels. We will finish this section with an application to a fault zone model.

To facilitate the discussion we compare the results for all three non-uniform models to the kernels for uniform media. The latter are shown in Fig. 2 at a lapse-time of 100 s for increasing scattering strengths. The columns from left to right show K_{tt}, K_{sc}

Table 1. Overview of intensities and fluxes.

Symbol	Description
I_s	Intensity from the source: forward intensity
I_d	Intensity from the detector: backward intensity
$I_\mathrm{s,d}^{\Delta\ell}$	Secondary and delayed intensity induced by a strong scattering region
$I_\mathrm{s,d}^\mathrm{b}$	Intensity along the ballistic path between source and detector
$\mathbf{J}_\mathrm{s}$	Energy flux from the source
$\mathbf{J}_\mathrm{d}$	Energy flux from the detector
$\mathbf{J}_\mathrm{s,d}^{\Delta\ell}$	Secondary and delayed energy flux induced by a strong scattering region
$\mathbf{J}_\mathrm{s,d}^\mathrm{b}$	Energy flux along the ballistic path between source and detector

and K_{dc}, respectively. The results obtained for a reference medium, with ℓ_1= 30 km, is shown at the top row. The scattering mean free path varies over orders of magnitude in the Earth, therefore we compare the reference medium with weaker scattering media. The middle and lower rows of Fig. 2 show the results for increasing ℓ: 2 $\times\ell_1$ and 8 $\times\ell_1$, respectively. The epicentral distance is set to R = 32 km. The numerical results shown in Fig. 2 will serve as guides to understand the more complex cases associated to non-uniform scattering properties.

4.1 Volcanic Setting

Fig. 3 shows the kernels for a source and receiver that are 47 km apart, at 40 s (upper row) and 80 s (lower row) lapse-times, in the vicinity of a volcano. The volcano, characterized by strong scattering, has a scattering mean free path of 2 km and a radius of 6 km. These values are based on the findings of Hirose et al. (2019) at the Sakurajima volcano in Japan. The surrounding crust has a weaker scattering strength with ℓ = 150 km, and for simplicity the intrinsic absorption is considered uniform with Q_i = 100.

A couple of observations stand out from Fig. 3. First, the travel-time and decorrelation kernels are very dissimilar. Second, the volcano appears to be a reflector for the intensities at early lapse-times. To explain these observations and improve the understanding of the kernels we will discuss all three kernels separately and compare them to

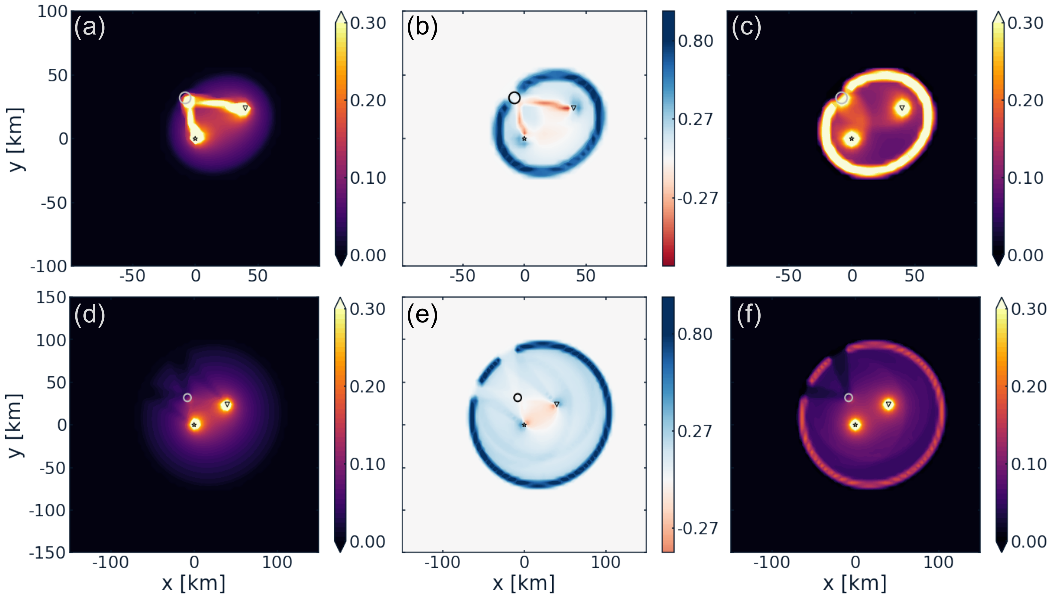

Figure 3. Sensitivity kernels for volcanic setting, for lapse-time of 40 s (upper) and 80 s (lower). The columns show K_{tt}, K_{sc} and K_{dc} respectively. The volcano is depicted as a circle with radius 6 km and $\ell_v = 2$ km, outside the volcano $\ell = 150$ km. The inter-source distance is approximately 47 km. Note that axis extent is not the same for 40 s (± 100 km) and 80 s (± 150 km). All kernels are normalised with respect to the maximum value. The color bar for K_{sc} is symmetric around zero.

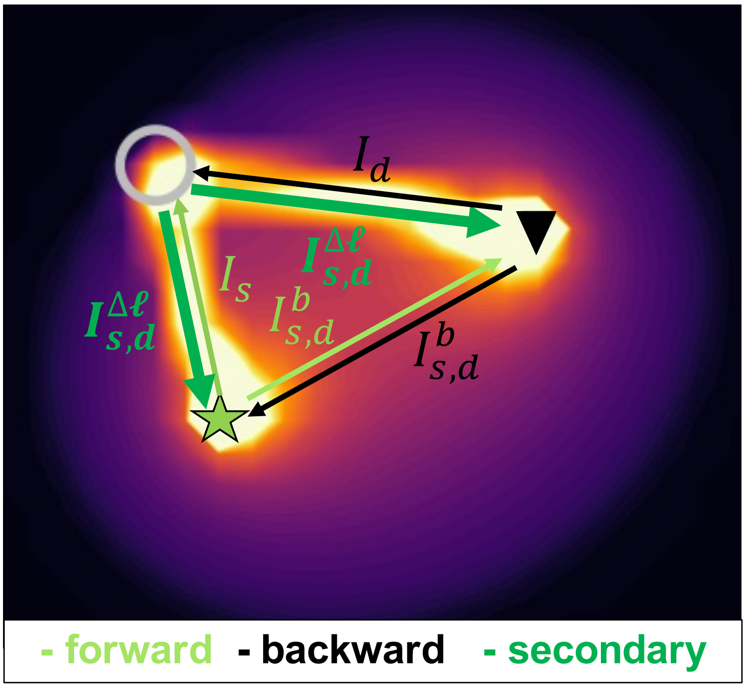

Figure 4. Depiction of the specific intensities controlling K_{tt} in a volcanic setting. The green star depicts the source and the black triangle the receiver. The former and the latter are referred to as source of forward and source of backward intensity, respectively. The grey circle shows the location of the volcano. Specific intensity I_s (I_d) propagates from the source of forward intensity (source of backward intensity) to the volcano, respectively. Back-scattered energy is indicated as $I_{\Delta\ell}$. It originates from one source and propagates via the volcano to the other source (and vice versa), but it also has an energy contribution coming from one source and scatters back to the same source. Both sources emit intensities into all directions, also on the direct path between them, as indicated by I_s and I_d.

the uniform model as reference, starting with the travel-time kernel, then the decorrelation kernel and finally the scattering kernel.

As defined in Eq. (1), K_{tt} is dependent on the dominant propagation direction of the waves. There are two specific intensities contributing to the travel-time kernel, coming from two different primary sources: (1) the forward intensity, from the source toward the perturbation; and (2) the backward intensity, from detector toward the perturbation. In the application part of this manuscript we refer to the first source as the "source of forward intensity" or "forward source", while the latter will be referred to as the "source of backward intensity" or "backward source" from hereafter.

Where the forward and backward intensities are simultaneously high and propagating in opposite direction, the travel-time kernel shows high sensitivities, as dictated by the convolution of specific intensities in the numerator of Eq. (1). In the uniform case, there are only two sources to be considered I_{s} and I_{d}. In the case of a localized perturbation with high scattering contrast, energy may be back-scattered by the heterogeneity, giving rise to a secondary and delayed intensity $I_{\mathrm{s,d}}^{\Delta\ell}$.

The key intensities for the volcanic setting are shown in the Fig. 4. As a result of the highly scattering volcano, specific intensities propagate from the forward source towards the volcano (green I_{s}), and scatter from the volcano to the source of backward intensity (green $I_{\mathrm{s,d}}^{\Delta\ell}$). Similarly, intensities propagate from the source of backward intensity to the volcano (black I_{d}) and from the volcano to the forward source (black $I_{\mathrm{s,d}}^{\Delta\ell}$). For 40 s lapse-time, we can therefore explain the high sensitivities on the paths connecting the sources via the volcano, by the high specific intensities that are opposite in direction on those paths. For the uniform case we observe higher sensitivities around and between the sources, especially for strong scattering media the sensitivity on the direct path between the sources increases (Fig. 2a). This direct path is less favorable in the volcanic setting, because the specific intensities are much higher on the paths that connect the sources of forward and backward intensity via the volcano. In other words, for early lapse-times the volcano acts as a secondary and delayed source of intensity and therefore promotes an additional path favorable to energy transport between the primary sources, which is not present in the uniform case. For later lapse-time (80 s; Fig. 3d), K_{tt} resembles its equivalent for a uniform medium. Yet the imprint of the volcano remains as the strongly scattering zone prevents ballistic energy to travel through and causes a "shadow" in the kernel for late lapse-times. The partly removed ballistic energies originating from both sources cause an 'M'-shaped shadow to appear, which deforms and gradually disappears with lapse-time. At later lapse-times the effect of the volcano starts to disappear as the portion of multiply scattered energy increases, resulting in a probability increase for two specific intensities to propagate in opposite directions in these areas. Animations of the three different kernels with increasing lapse-time for the volcanic setting can be found in the supporting information, Movie S1-S3.

The decorrelation kernels appear rather different from their travel-time counterparts. Indeed, Eq. (2) shows that K_{dc} does not depend on the specific intensities, but on the mean intensities instead. The decorrelation kernel will thus be high where the mean intensities emitted by the forward and backward sources are simultaneously high. This condition is far less stringent than the analogous one for the travel-time kernel. For this reason the travel-time and decorrelation kernel are dissimilar. The K_{dc} for the volcanic case at early lapse-time (40 s; Fig. 3c) shows high sensitivity around the sources and on the single scattering ellipse. Additionally, high sensitivity can be observed in the halos surrounding the forward source and volcano, and the backward source and volcano, respectively. Energy becomes rapidly diffuse when it enters into the volcano, therefore the high intensities inside the volcano are on the side that faces the sources; hence a bend in the single scattering ellipse can be observed (Fig. 3c). For later lapse-times (80 s; Fig. 3f), K_{dc} appears similar to the uniform K_{dc} (Fig. 2i). Nevertheless, the imprint of the strongly scattering volcano remains, causing a shadow on the single-scattering ellipse of the decorrelation kernel.

The last kernel to be considered is the scattering kernel (Fig. 3 b&e). In order to understand its structure in the vicinity of a volcano, we will first discuss the pattern of K_{sc} for the uniform case (e.g. Fig. 2e). As mentioned in Section 2, the scattering kernel has positive and negative sensitivities. The signs in the kernels can be understood in the following way. If we imagine point sources at the locations of the source and detector that inject energy into the medium at time $t = 0$. The energy transport gives rise to fluxes going from a source of forward intensity to a source of backward intensity (and vice versa). At late lapse-times, which is at several scattering mean free times τ (where $\tau = \ell/c$ with c as wave velocity), the energy is diffuse. Previously, it has been shown in the literature that in the diffusion regime the scattering kernel is controlled by the scalar product of the energy flux vectors ($\boldsymbol{J}$) for sources located at the position of the forward/backward

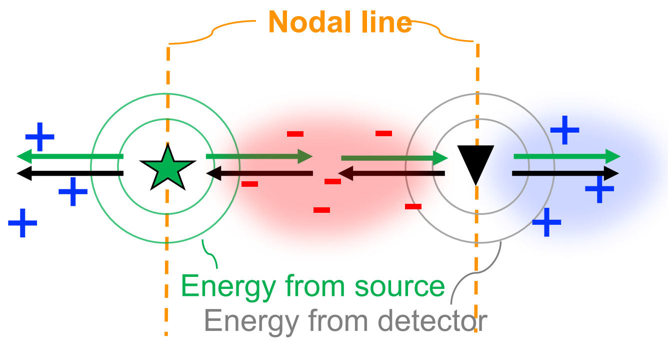

Figure 5. Graphical interpretation of the fluxes explaining the pattern of the scattering kernel for a uniform scattering medium. Energy from the source (green star) is emitted in all directions, indicated by the green circles. The green arrows depict the fluxes along the line connecting the source and detector. Similarly, energy from the detector (black triangle) is emitted in all directions, indicated by the gray circles. The black arrows depict fluxes from the detector in the source-detector line. In the space between source and detector the fluxes have opposite direction, resulting in negative sensitivity (red '-'). In the outside spaces, the fluxes from source and detector have similar directions, resulting in positive sensitivity to scattering (blue '+'). The nodal lines are depicted by the orange dashed line.

intensity sources (e.g. Arridge, 1995; Wilson & Adam, 1983; Mayor et al., 2014):

$$\lim_{t\to+\infty} K_{\text{sc}}\left(\mathbf{r};\mathbf{r}';\mathbf{r}_0;t\right) = D(1-g)\int_0^t \mathbf{J}_{\mathbf{fwd}}\left(\mathbf{r}';\mathbf{r};t-t'\right)\cdot\mathbf{J}_{\mathbf{bwd}}\left(\mathbf{r}';\mathbf{r}_0;t'\right)\mathrm{d}t' \qquad (12)$$

with g denoting the mean cosine of the scattering angle. Note that Eq. (12) is not strictly valid quantitatively, although qualitatively it is correct. Hence, Eq. (12) is rather an approximate than an exact formula, which in practice explains the pattern of the scattering kernel accurately. It contains the essential physics and therefore we employ this formulation heuristically to analyse our results. Fig. 5 shows a schematic diagram of the fluxes in the scattering kernel for a uniform medium. The energy flux from the source flows away in all directions from the source and similarly for the detector. On the direct path between source and detector, these fluxes have opposite direction while on the outside the fluxes have similar directions. As a consequence of the scalar product in Eq. (12), the fluxes in opposite direction lead to an area of negative sensitivity to scattering on the direct path. Here, the probability of energy reaching the other source is decreased. On the outer side of the direct path between the sources, there is a positive sensitivity due to the scalar product of the fluxes in similar direction. In these positive areas the probability of energy reaching the other detector is increased. The line that divides the positive and the negative sensitivities in the vicinity of the source/detector is referred to as the nodal line (Fig. 5). To describe the pattern of the scattering kernel in more detail we imagine placing additional scatterers at three locations in Fig. 5. If an extra scatterer would have been placed left of the forward intensity source, the chances of additional energy reaching the backward intensity source would have been increased due to the possibility of back-scattering. Due to reciprocity, this same argument holds for an additional scatterer located right of the backward source. On the other hand, negative scattering sensitivity between the two sources indicates that if an additional scatterer would have been placed in the red area, the probability of energy coming from one source and reaching the other source would decrease.

Now that we have discussed the positive and negative signs in K_{sc} for a uniform medium we continue the discussion about the volcanic case. K_{sc} will be high in absolute value where the actual energy fluxes are simultaneously large and aligned, either parallel or anti-parallel. Consequently, an additional energy transport channel in the scattering kernel for early lapse-times (40 s; Fig. 3b) appears, connecting the two sources via the volcano. The negative sensitivity on the direct path between the sources is also present, albeit weaker than on the path via the volcano. Similarly as for K_{tt}, this is due to smaller energy current vectors on the direct path. Furthermore, we can observe similarities between the decorrelation and the scattering kernel, for both the early and late lapse-times. In particular, the single scattering ellipse and the halos of high sensitivity between either source and volcano, which are also present in K_{dc}, can be observed in Fig. 3(b & e). Although K_{sc} for the volcanic setting at late lapse-time (80 s) resembles its equivalent for a uniform model, the effect of the volcano remains.

4.2 Two Half-spaces Setting

In the northeastern region of Honshu, Japan, Yoshimoto et al. (2006) estimated the spatial distribution of attenuation. These authors found that the contrast of properties between the front-arc and the back-arc is approximately equal to two for both absorption and scattering. With this in mind, we explore the effect of non-uniform scattering properties on the coda wave sensitivities, in a medium composed of two half-spaces. A tectonic setting with a strike-slip fault that caused two different materials on each side of the fault to be in contact may also be considered in this context. For all half-space

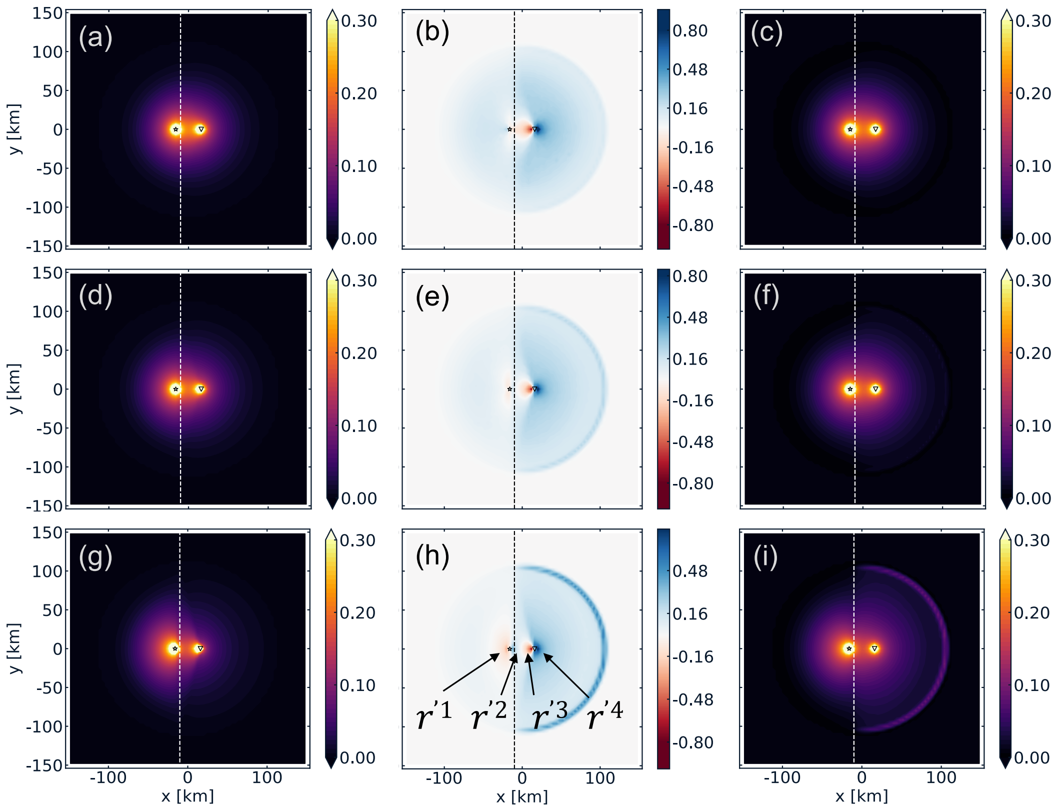

Figure 6. Sensitivity kernels for two half-spaces at 100 s lapse-time. The columns show K_{tt}, K_{sc} and K_{dc}, respectively. The left half-space has a fixed scattering mean free path of ℓ_1. The scattering mean free path in the right half-space increases from top to bottom: $2\times\ell_1$, $3\times\ell_1$, $8\times\ell_1$, with $\ell_1 = 30$ km. The source-detector distance R_0 is set to 32 km. The annotations r'^1-r'^4 point to negative, positive, negative and positive sensitivity along the line connecting source and detector, respectively. All kernels are normalised with respect to the maximum value. Note that for K_{sc} the color bar is symmetric around zero, with red as negative and blue as positive sensitivities, respectively.

models, ℓ_1 is the smallest scattering mean free path we consider, it is kept constant at 30 km and consistently on the left side of the model. The right half-space has weaker scattering ($\ell_1 < \ell_2$), where ℓ_2 is chosen to differ by a factor of 2, 3, or 8 from ℓ_1. The interface delimiting the two half-spaces coincides exactly with the boundary between two pixels. d represents the distance from the forward intensity source to this interface.

The sensitivity kernels with sources in opposite half-spaces are shown in Fig. 6, for t =100 s. From the top to the bottom row, we show the results for increasing scattering contrast between ℓ_1 (the reference half-space, on the left) and ℓ_2 (the right half space): $\ell_2 = 2 \times \ell_1$ (upper), $\ell_2 = 3 \times \ell_1$ (middle) and $\ell_2 = 8 \times \ell_1$(lower). The dashed line, placed at 6 km from the source of forward intensity, depicts the boundary between the two half-spaces. The inter-source distance is the same as for the uniform cases, $R = 32$ km. We can observe that all three kernels for all degrees of scattering contrast are asymmetric, with the asymmetry intensifying as the contrast between ℓ_1 and ℓ_2 increases. In the travel-time kernel there is a strong effect of back-scattering, especially for the case where $\frac{\ell_2}{\ell_1}$ = 8 (Fig. 6 g). The sensitivities appear higher in the strong scattering half-space. For the decorrelation kernels we can observe the increased difference between dominant transport regimes for increasing scattering contrasts. For example in Fig. 6 (i) the dominant type of wave propagation in the left half-space is diffusion. Therefore, the mean intensity and thus the sensitivity is concentrated in a larger area around the source. However, in the right half-space the propagation regime is essentially ballistic, consequently, strong sensitivities can be observed on the single scattering ellipse. The most striking observation from Fig. 6 is the "flipped" pattern in the scattering kernels (w.r.t. the pattern for the uniform case), for $\frac{\ell_2}{\ell_1} \geq 3$ (Fig. 6 e and h). In the strong scattering half-space (with ℓ_1), the sensitivity to an additional scatterer left of the source is negative ($r^{'1}$ in panel h), while it was positive for the uniform case (Fig. 2e). On the other side of the source ($r^{'2}$) it is positive, while for the uniform case it was negative. The sensitivity to an additional scatterer in the weaker scattering half-space (with ℓ_2) appears similar to that for the uniform case in the vicinity of the source, with negative sensitivity at $r^{'3}$ and positive at $r^{'4}$, regardless of the scattering strength or contrast.

Fig. 6 shows that for a certain scattering contrast, the pattern of the scattering kernel changes significantly w.r.t. the uniform kernel. As explained for the volcanic setting, this is due to the active fluxes: from the forward source, $\mathbf{J}_{\mathrm{s}}$, and the backward source, $\mathbf{J}_{\mathrm{d}}$, but also the flux governed by the contrast in scattering $\mathbf{J}_{\mathrm{s,d}}^{\Delta\ell}$. In order to improve our understanding of the "flipped" scattering kernel for models with two half-spaces and to gain more insight into the factors that affect the active fluxes we perform two additional tests. In one test we take four models in which the scattering distribution of the medium is fixed, but the location of one of the sources rotates. In another parametric test we investigate the effect of several parameters on the magnitude and directivity of each flux.

If we denote the part of $\mathbf{J}_{\mathrm{s}}$ ($\mathbf{J}_{\mathrm{d}}$) flowing in the direction of the backward source (forward source), respectively, as the direct flux $\mathbf{J}_{\mathrm{s,d}}^{\mathrm{b}}$. Then the flux at the sources is a com-

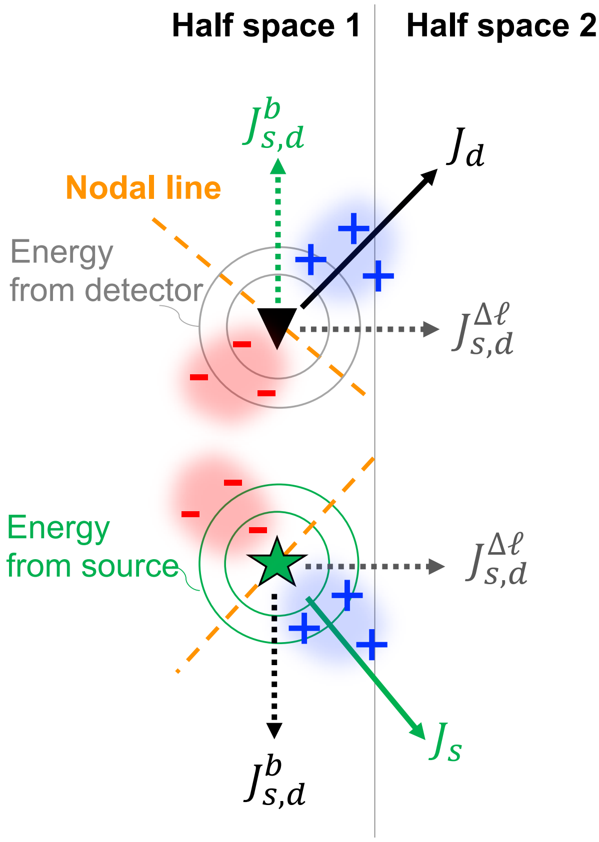

Figure 7. Graphical representation of the active fluxes and K_{sc} in case of a medium with two half-spaces. The fluxes shown in green are from the source of forward intensity. The flux $\mathbf{J}^{\mathrm{b}}_{\mathrm{s,d}}$ in green (black) is the part of the energy from the forward source (backward source) in the direction of the backward source (forward source), respectively. The resulting flux at the forward source, $\mathbf{J}_{\mathrm{s}}$ shown in green, (backward source, $\mathbf{J}_{\mathrm{d}}$ shown in black) has contributions from $\mathbf{J}^{\mathrm{b}}_{\mathrm{s,d}}$ and $\mathbf{J}^{\Delta\ell}_{\mathrm{s,d}}$, respectively. $\mathbf{J}^{\Delta\ell}_{\mathrm{s,d}}$ is the flux induced by the contrast in scattering. The nodal line, depicted in orange, separates positive and negative sensitivity to scattering and is perpendicular to the resulting energy flux.

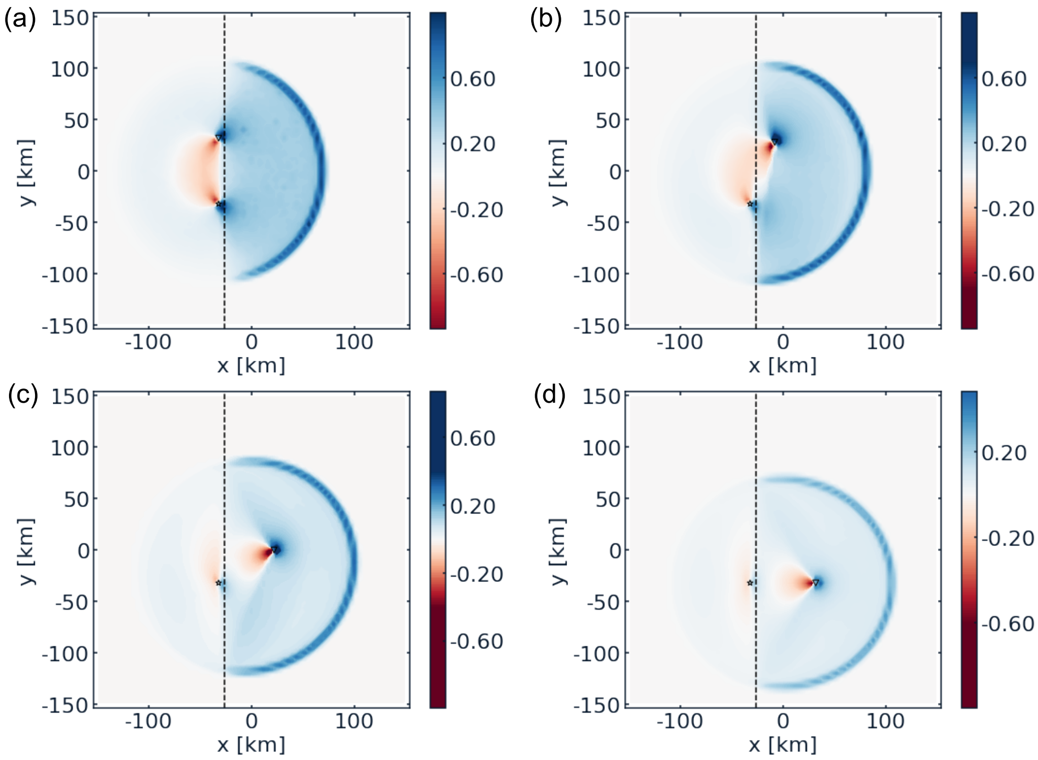

Figure 8. Sensitivity kernels for a half-space setting at 100 s lapse-time. The scattering mean free path for the left (right) half-space is fixed for all panels at ℓ_1 ($8\times\ell_1$), respectively. The orientation of the line connecting the sources changes gradually from parallel to the boundary to perpendicular to the boundary, from (a) - (d), respectively. To enhance visibility of the kernel pattern the inter-source distance is larger, with R = 2 x R_0. The distance of the leftmost source from the boundary is fixed at 6 km.

bination of $\mathbf{J}^{\mathrm{b}}_{\mathrm{s,d}}$ and $\mathbf{J}^{\Delta\ell}_{\mathrm{s,d}}$, as illustrated in Fig. 7. For the situation in Fig. 7, the magnitude of $\mathbf{J}^{\Delta\ell}_{\mathrm{s,d}}$ depends on the contrast of scattering between both half-spaces. The orientation of $\mathbf{J}^{\Delta\ell}_{\mathrm{s,d}}$ is perpendicular to the boundary of scattering and is directed from the stronger scattering half-space towards the weaker scattering half-space. The orientation of $\mathbf{J}^{\mathrm{b}}_{\mathrm{s,d}}$ depends on the positions of the sources, while its magnitude depends on the inter-source distance and lapse-time.

Fig. 8 demonstrates how the direct flux and the flux induced by the scattering contrast contribute to the pattern of the scattering kernel. In all four panels the scattering contrast is fixed, with $\frac{\ell_2}{\ell_1} = 8$, and the orientation of $\mathbf{J}^{\Delta\ell}_{\mathrm{s,d}}$ is perpendicular to the scattering boundary. From panel (a) to (d) the location of the upper source changes, but its

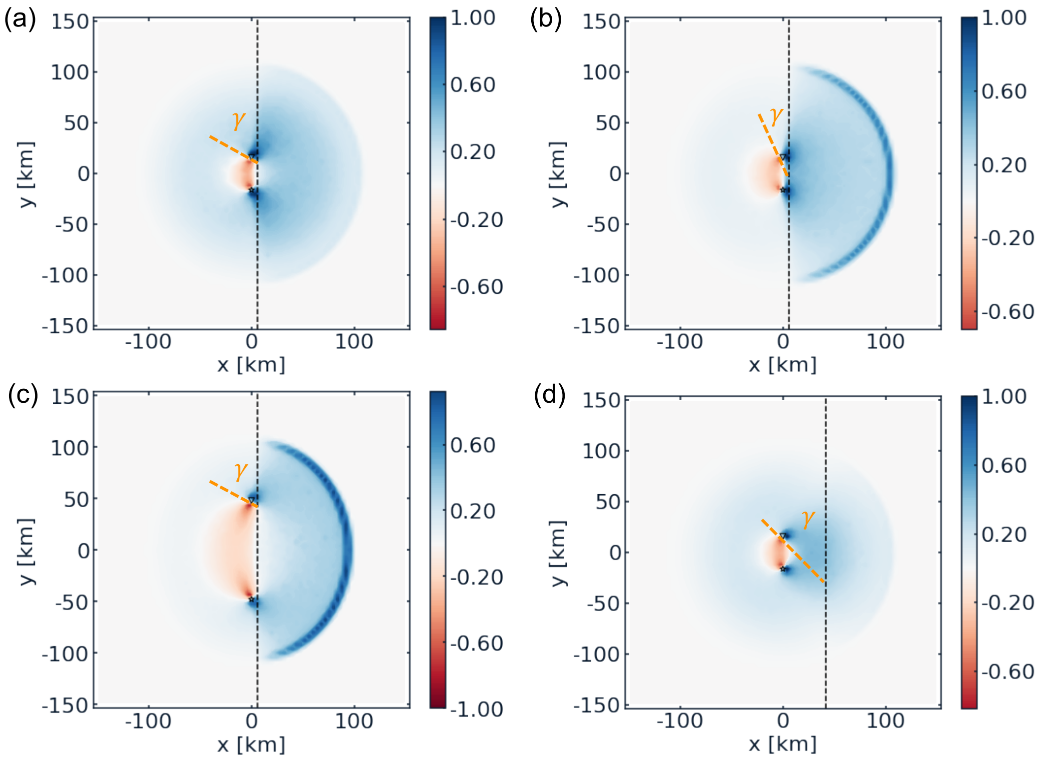

Figure 9. Sensitivity kernels for a half-space setting at 100 s lapse-time. Scattering mean free path of left half-space for all panels is ℓ_1= 30 km. Source and detector are placed parallel to half-space boundary. (a) ℓ of right half-space is $2{\times}\ell_1$, $R = R_0 = 32$ km and distance to half-space boundary $d = 6$ km. (b) ℓ of right half-space is $8{\times}\ell_1$, $R = R_0$ and $d = 6$ km. (c) ℓ of right half-space is $8{\times}\ell_1$, $R = 3\times R_0$ and $d = 6$ km. (d) ℓ of right half-space is $8{\times}\ell_1$, $R = R_0$ and $d = 42$ km. γ denotes the angle between the nodal line (orange dashed line) and the half-space boundary. Note that the color bar is symmetric around zero.

distance to the lower source is kept constant at $R = 64$ km ($2\times R_0$). We rotate the line connecting the two sources from parallel to the boundary (Fig. 8a) to perpendicular to the boundary (Fig. 8d). This causes the orientation of $\mathbf{J}^{\mathrm{b}}_{\mathrm{s,d}}$ to rotate and therefore the kernel pattern to change from a "twisted" version of the uniform kernel (Fig. 8a and Fig. 7) to a kernel with completely opposite sensitivity in the stronger scattering half-space (w.r.t. the uniform kernel), as we have already seen in Fig. 6 (h).

There are multiple parameters that affect either direction or amplitude of $\mathbf{J}^{\mathrm{b}}_{\mathrm{s,d}}$, $\mathbf{J}^{\Delta\ell}_{\mathrm{s,d}}$, and/or the relative contribution of both fluxes and therefore the kernels; a selection is shown in Fig. 9. The effect in scattering contrast, and as a consequence on $\mathbf{J}^{\Delta\ell}_{\mathrm{s,d}}$, can be seen when comparing Fig. 9 (a) where $\ell_2 = 2 \times \ell_1$ with Fig. 9 (b) where $\ell_2 = 8 \times \ell_1$. If ℓ_2 in the right half-space increases from 2 (panel a) to 8 (panel b) the kernel looks more asymmetric. Not only is the sensitivity partly focused on the singly scattering ellipse for the weaker scattering half-space, but also in the vicinity of both sources we observe a deformation of the kernel w.r.t. the uniform case. The angle γ, between the half-spaces boundary and the nodal line, decreases. Note that the nodal line is always perpendicular to the resulting flux at the source, as show in Fig. 5 and 7. The change in γ is due to the larger $\mathbf{J}^{\Delta\ell}_{\mathrm{s,d}}$, which is induced by the increasing scattering contrast. This alters the magnitude and direction of the flux, despite the unchanged orientation of the individual fluxes $\mathbf{J}^{\Delta\ell}_{\mathrm{s,d}}$ and $\mathbf{J}^{\mathrm{b}}_{\mathrm{s,d}}$. Another parameter that affects the pattern of K_{sc} is the inter-source distance, which directly affects the contribution of $\mathbf{J}^{\mathrm{b}}_{\mathrm{s,d}}$ to the flux. For a larger R the angle γ increases as can be observed when comparing the kernel for $R = R_0$ (panel b) to $R = 3 \times R_0$ (panel c).

Additionally, when comparing Fig. 9(b) to Fig. 9(d) we observe that the distance of the sources to the boundary of scattering contrast, d, also plays an important role in the pattern of the kernel. The kernel for larger d (panel d) appears more similar to the kernel for uniform scattering (e.g. Fig. 2) than the kernel for smaller d (panel b). Thus the effect of the non-uniformity decreases with increasing d. The lack of sensitivity on the singly scattering ellipse (panel d) is a consequence of the energy being already diffuse before reaching the weaker scattering half-space. The two tests discussed above show that we can improve our interpretation of the scattering kernels by understanding the actual fluxes.

Finally, Fig. 10 shows the effect of non-uniform scattering strength on the decorrelation, travel-time and scattering kernels for a model with sources far away from a boundary of scattering contrast. The sources are placed at a large distance (58 and 90 km) from the contrast of scattering inside the weaker scattering half-space, where $\ell_1 = 30$ km and $\ell_2 = \ell_1 \times 8$ km. In the travel-time kernel (Fig. 10a) the strong backscattering effect, caused by the contrast in scattering, results in a larger sensitivity towards the strong scattering half-space. This is due to the overlap of intensities from the sources, which go toward the left, with the reflected intensity from the half-space that goes to the right. This travel-time kernel is rather different from the travel-time kernel for the uniform case (Fig. 2), where the sensitivity would have solely been around the two sources. The decorrelation kernel shows concentrated sensitivities on the single scattering ellipse, as we have

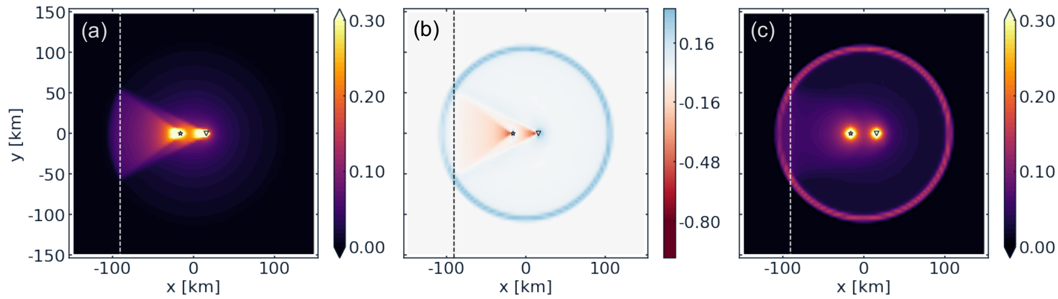

Figure 10. Sensitivity kernels for a model with two half-spaces at 100 s lapse-time, for a setting where the sources are far away from the boundary of scattering contrast (58 and 90 km, respectively). The scattering mean free path in the right half-space is 8 $\times$ ℓ_1, where $\ell_1 = 30$ km. The columns show K_{tt}, K_{sc} and K_{dc}, respectively. All kernels are normalised with respect to the maximum value. The color bar for K_{sc} is symmetric around zero.

seen in the uniform weakly scattering medium. The sensitivity of the single scattering ellipse in the strong scattering half-space is lower due to the stronger diffusion of energy in the left half-space. Furthermore, higher sensitivities can be explained between the boundary of scattering on the one hand, and the source on the other hand, by the increase of mean intensities in those areas. Fig. 10 (b) shows that the impact on the scattering kernel is also significant. The contribution of the specific intensities, as in the travel-time kernel, is clearly visible and results in strong negative sensitivities towards the stronger scattering half-space. Furthermore, we can observe the single scattering ellipse, as we have seen in the decorrelation kernels.

The results in Fig. 10 thus show that even at large distance from a boundary of scattering contrast the effect of non-uniform scattering properties on the sensitivity kernels can be significant. It is therefore important to have knowledge about the distribution of scattering for a large area around one's area of interest, in order to locate changes of the subsurface correctly.

4.3 Fault Zone Setting

The last application we consider is a fault zone setting. The parameters are based on findings for the North Anatolian Fault (van Dinther et al., 2020). We consider a narrow fault zone of width = 6.25 km, with $\ell = 10$ km inside and $\ell = 150$ km outside. Fig. 11 shows the resulting kernels for 65 s (upper) and 100 s (lower) lapse-times, respectively.

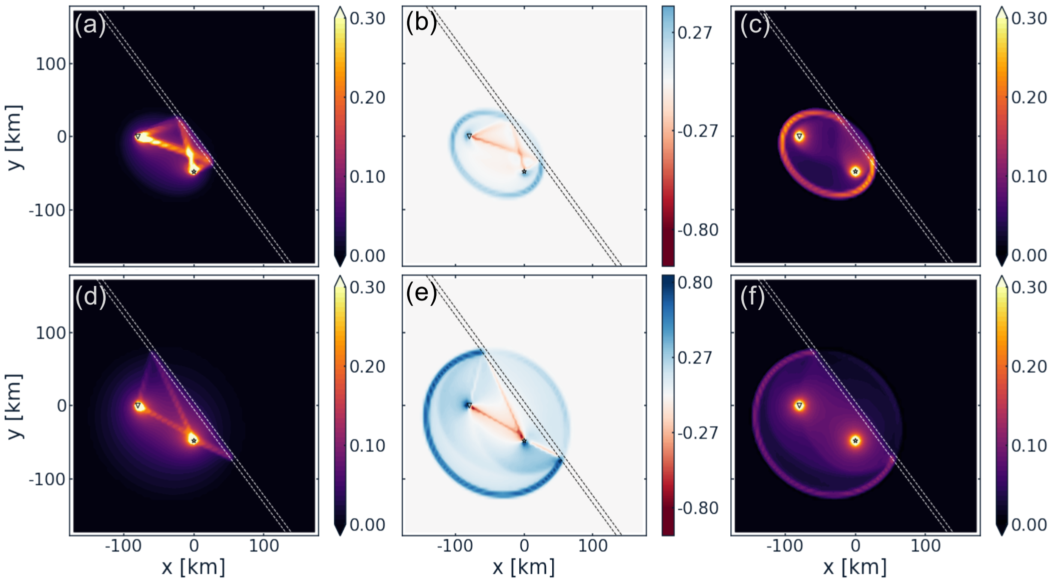

Figure 11. Sensitivity kernels for fault zone setting with both sources on one side of the fault (dashed lines), for lapse-times of 65 s (upper) and 100 s (lower). The columns show K_{tt}, K_{sc} and K_{dc}, respectively. The width of the fault zone is 6.25 km. The scattering mean free path in and outside the fault zone are $\ell_{FZ} = 10$ km and $\ell = 150$ km, respectively. The distance between the two sources is approximately 93 km. All kernels are normalised with respect to the maximum value. The color bar for K_{sc} is symmetric around zero.

Note that due to the inter-source distance of ~ 93 km in combination with a seismic velocity of 2.1 km s^{-1}, the earliest lapse-times for which the kernels are evaluated are around 45 s. The travel-time and scattering kernels may appear more complex than kernels shown for the other non-uniform media. In the travel-time kernel we observe two additional two-legged transport paths that connect the source and the detector. They are actually generated at the intersections of the single scattering ellipse with the fault zone where the strong scattering acts as secondary sources. For each of these paths, the backward and forward intensities are in exactly opposite directions. As explained for the K_{tt} of other models, the overlap of the specific intensities of either primary and/or secondary sources (in opposite direction) causes high sensitivities in the travel-time kernels. For the fault zone setting, this results in multiple pathways that are favorable for energy transport between the two primary sources (Fig. 11 a & d). For early lapse-time (65 s) we can observe a spot with even higher concentrated sensitivity, at the intersection of the energy transport paths. Furthermore, the geometry of these additional paths between the primary sources changes with lapse-time, as can be more clearly observed in the animations in the supporting information (Movie S4).

Fig. 11 (b & e) show similar observations for the scattering kernel, where the simultaneously large and aligned energy fluxes create additional energy transport paths between the primary sources in the scattering kernel. The contribution of the high mean intensities is also visible in K_{sc}, which is similar to the halos of high sensitivities that are formed around the sources in the decorrelation kernel. Again K_{dc} does not resemble K_{tt}, and shows that the highly diffusive fault zone acts as a barrier for energy passing through. Hence, the mean intensity is low on the right side of the fault zone in Fig. 11 (f). In the supporting information, additional animations for K_{sc} (Movie S5) and K_{dc} (Movie S6) with lapse-time for the fault zone setting can be found.

5 Concluding Remarks

For monitoring the temporal evolution of the subsurface we need coda wave sensitivity kernels that linearly relate observed changes in recordings to physical medium changes. Here we compute travel-time, scattering and decorrelation kernels based on a flexible Monte Carlo method, which enables us to include non-uniformly distributed scattering properties. In this work we have shown that non-uniform scattering properties can have a profound and non-intuitive effect on coda wave sensitivity kernels. Hence, it could be misleading to overlook the distribution of scattering properties in monitoring applications. The actual impact on the kernels depends on a combination of lapse-time and mean free time, it is therefore important to have knowledge about the geology and an estimate on the scattering mean free path in the wider region that is targeted to be monitored.

There are two unique energy sources considered in the kernel computation for either uniform or non-uniform cases, namely the one from the source and the one from the detector, also referred to as the source of forward intensity and of backward intensity, respectively. Yet we have shown that due to non-uniform scattering properties additional energy transport channels can appear between the two sources, which do not exist in the case of a uniform scattering medium. Therefore, the sensitivity kernels for non-uniform scattering media can appear rather complex. The physical interpretation of the three different kernels is as follows: (1) the decorrelation kernel is the most straightforward to interpret and has high sensitivities where the mean intensities are high; (2) the travel-time kernel requires that the forward and backward specific intensities are simultaneously large and in opposite direction; (3) the scattering kernel combines the properties of both the decorrelation and travel-time kernel and has high absolute sensitivities where the energy fluxes are simultaneously large and parallel or anti-parallel. Furthermore, the pattern of positive and negative sensitivities in the scattering kernel is controlled by the scalar product of the current fluxes from the forward and backward sources. The interpretation of the scattering kernel is more intuitive when considering the dominant contributions to the energy fluxes.

There are two types of fluxes contributing to the resulting fluxes around the two sources: (1) the direct flux between the forward and backward sources, and (2) the flux induced by the non-uniformity of scattering strength. The direction and magnitude of these two fluxes in turn depend on several parameters including distance from the boundary of scattering contrast, inter-source distance, orientation of the sources w.r.t. each other and the scattering contrast. In order to fully understand the scattering kernels, it requires knowledge of these actual fluxes, primarily from the sources and secondarily governed by the distribution of scattering, because the magnitude and direction of the fluxes may lead to additional pathways for energy transport between the two unique sources. Regarding Eq. (12), the interpretation of the energy propagation as energy fluxes is only valid in the diffusion regime. Yet with our findings it appears that this interpretation may be extended to any propagation regime. However, more rigorous mathematical work is required to prove this.

Finally, this study visually demonstrates the difference between travel-time and decorrelation kernels, although mathematically this has already been shown by Margerin et al. (2016). Therefore, it emphasises that one needs to be careful with uncontrolled approximations. In our context, generic formulas derived in the diffusion regime cannot be extended to the ballistic regime by simply substituting the heat diffusion Green's function with a more accurate Green's function derived from radiative transport theory. The key issue is that diffusion theory does not allow to distinguish between decorrelation and travel-time kernels because it relies on average intensities. This deficiency cannot be fixed a-posteriori.

Acknowledgments

We acknowledge the support from the European Research Council (ERC) under the European Union's Horizon 2020 research and innovation program (grant agreement No 742335, F-IMAGE). This work was granted access to the HPC resources of CALMIP supercomputing center under the allocation 2020-p19038, where the majority of the simulations have been run. Some of the computations presented in this paper were performed using the CIMENT infrastructure (https://ciment.ujf-grenoble.fr), which is supported by the Rhône-Alpes region (grant CPER07_13 CIRA: (http://www.ci-ra.org) and France-Grille (http://www.france-grilles.fr)). The code used for the numerical simulations is currently being archived and will be made publicly available on https://doc.archives-ouvertes.fr/en/.

References

Arridge, S. R. (1995). Photon-measurement density functions. part I: Analytical forms. *Applied Optics*, *34*(31), 7395–7409.

Barajas, A. (2021). *Imaging for scattering properties of the crust: body to surface waves coupling* (Unpublished doctoral dissertation).

Brenguier, F., Campillo, M., Hadziioannou, C., Shapiro, N. M., Nadeau, R. M., & Larose, E. (2008). Postseismic relaxation along the San Andreas fault at Parkfield from continuous seismological observations. *science*, *321*(5895), 1478–1481.

Brenguier, F., Rivet, D., Obermann, A., Nakata, N., Boué, P., Lecocq, T., . . .

Shapiro, N. (2016). 4-D noise-based seismology at volcanoes: Ongoing efforts and perspectives. *Journal of Volcanology and Geothermal Research*, *321*, 182–195.

Chen, J. H., Froment, B., Liu, Q. Y., & Campillo, M. (2010). Distribution of seismic wave speed changes associated with the 12 may 2008 mw 7.9 wenchuan earthquake. *Geophysical Research Letters*, *37*(18).

Duran, A., Planès, T., & Obermann, A. (2020). Coda-wave decorrelation sensitivity kernels in 2-d elastic media: a numerical approach. *Geophysical Journal International*, *223*(2), 934–943.

Gaebler, P., Eken, T., Bektaş, H. Ö., Eulenfeld, T., Wegler, U., & Taymaz, T. (2019). Imaging of shear wave attenuation along the central part of the North Anatolian Fault Zone, Turkey. *Journal of Seismology*, *23*(4), 913–927.

Hillers, G., Husen, S., Obermann, A., Planès, T., Larose, E., & Campillo, M. (2015). Noise-based monitoring and imaging of aseismic transient deformation induced by the 2006 Basel reservoir stimulation. *Geophysics*, *80*(4), KS51–KS68.

Hillers, G., T. Vuorinen, T. A., Uski, M. R., Kortström, J. T., Mäntyniemi, P. B., Tiira, T., . . . Saarno, T. (2020). The 2018 geothermal reservoir stimulation in Espoo/Helsinki, southern Finland: Seismic network anatomy and data features. *Seismological Research Letters*, *91*(2A), 770–786.

Hirose, T., Nakahara, H., & Nishimura, T. (2017). Combined use of repeated active shots and ambient noise to detect temporal changes in seismic velocity: Application to Sakurajima volcano, Japan. *Earth, Planets and Space*, *69*(1), 42.

Hirose, T., Nakahara, H., & Nishimura, T. (2019). A passive estimation method of scattering and intrinsic absorption parameters from envelopes of seismic ambient noise cross-correlation functions. *Geophysical Research Letters*, *46*(7), 3634–3642.

Hoshiba, M. (1991). Simulation of multiple-scattered coda wave excitation based on the energy conservation law. *Physics of the Earth and Planetary Interiors*, *67*(1-2), 123–136.

Kanu, C., & Snieder, R. (2015a). Numerical computation of the sensitivity kernel for monitoring weak changes with multiply scattered acoustic waves. *Geophysical Supplements to the Monthly Notices of the Royal Astronomical Society*, *203*(3), 1923–1936.

Kanu, C., & Snieder, R. (2015b). Time-lapse imaging of a localized weak change with multiply scattered waves using numerical-based sensitivity kernel. *Journal of Geophysical Research: Solid Earth*, *120*(8), 5595–5605.

Lux, I., & Koblinger, L. (1991). *Monte Carlo particle transport methods: neutron and photon calculations*. CRC Press.

Mao, S., Campillo, M., van der Hilst, R. D., Brenguier, F., Stehly, L., & Hillers, G. (2019). High temporal resolution monitoring of small variations in crustal strain by dense seismic arrays. *Geophysical Research Letters*, *46*(1), 128–137.

Margerin, L. (2005). Introduction to radiative transfer of seismic waves. *Geophysical Monograph-American Geophysical Union*, *157*, 229.

Margerin, L., Bajaras, A., & Campillo, M. (2019). A scalar radiative transfer model including the coupling between surface and body waves. *Geophysical Journal International*, *219*(2), 1092–1108.

Margerin, L., Campillo, M., & Van Tiggelen, B. (2000). Monte Carlo simulation of multiple scattering of elastic waves. *Journal of Geophysical Research: Solid Earth*, *105*(B4), 7873–7892.

Margerin, L., Planès, T., Mayor, J., & Calvet, M. (2016). Sensitivity kernels for coda-wave interferometry and scattering tomography: theory and numerical evaluation in two-dimensional anisotropically scattering media. *Geophysical Journal International*, *204*(1), 650–666.

Mayor, J., Margerin, L., & Calvet, M. (2014). Sensitivity of coda waves to spatial variations of absorption and scattering: radiative transfer theory and 2-D examples. *Geophysical Journal International*, *197*(2), 1117–1137.

Mordret, A., Jolly, A., Duputel, Z., & Fournier, N. (2010). Monitoring of phreatic eruptions using interferometry on retrieved cross-correlation function from ambient seismic noise: Results from Mt. Ruapehu, New Zealand. *Journal of Volcanology and Geothermal Research*, *191*(1-2), 46–59.

Obermann, A., Kraft, T., Larose, E., & Wiemer, S. (2015). Potential of ambient seismic noise techniques to monitor the St. Gallen geothermal site (Switzerland). *Journal of Geophysical Research: Solid Earth*, *120*(6), 4301–4316.

Obermann, A., Planès, T., Hadziioannou, C., & Campillo, M. (2016). Lapse-time-dependent coda-wave depth sensitivity to local velocity perturbations in 3-D heterogeneous elastic media. *Geophysical Journal International*, *207*(1), 59–66.

Obermann, A., Planes, T., Larose, E., & Campillo, M. (2013). Imaging preeruptive and coeruptive structural and mechanical changes of a volcano with ambient seismic noise. *Journal of Geophysical Research: Solid Earth*, *118*(12), 6285–6294.

Obermann, A., Planes, T., Larose, E., & Campillo, M. (2019). 4-D imaging of subsurface changes with coda waves: Numerical studies of 3-D combined sensitivity kernels and applications to the m_w 7.9, 2008 Wenchuan earthquake. *Pure and Applied Geophysics*, *176*(3), 1243–1254.

Obermann, A., Planès, T., Larose, E., Sens-Schönfelder, C., & Campillo, M. (2013). Depth sensitivity of seismic coda waves to velocity perturbations in an elastic heterogeneous medium. *Geophysical Journal International*, *194*(1), 372–382.

Ogiso, M. (2019). A method for mapping intrinsic attenuation factors and scattering coefficients of s waves in 3-d space and its application in southwestern japan. *Geophysical Journal International*, *216*(2), 948–957.

Paasschens, J. (1997). Solution of the time-dependent Boltzmann equation. *Physical Review E*, *56*(1), 1135.

Pacheco, C., & Snieder, R. (2005). Time-lapse travel time change of multiply scattered acoustic waves. *The Journal of the Acoustical Society of America*, *118*(3), 1300–1310.

Pacheco, C., & Snieder, R. (2006). Time-lapse traveltime change of singly scattered acoustic waves. *Geophysical Journal International*, *165*(2), 485–500.

Peng, Z., & Ben-Zion, Y. (2006). Temporal changes of shallow seismic velocity around the Karadere-düzce branch of the north Anatolian fault and strong ground motion. *Pure and Applied Geophysics*, *163*(2-3), 567–600.

Planès, T., Larose, E., Margerin, L., Rossetto, V., & Sens-Schönfelder, C. (2014). Decorrelation and phase-shift of coda waves induced by local changes: multiple scattering approach and numerical validation. *Waves in Random and Complex Media*, *24*(2), 99–125.

Poupinet, G., Ellsworth, W., & Frechet, J. (1984). Monitoring velocity variations in the crust using earthquake doublets: An application to the Calaveras Fault, California. *Journal of Geophysical Research: Solid Earth*, *89*(B7), 5719–5731.

Rivet, D., Campillo, M., Radiguet, M., Zigone, D., Cruz-Atienza, V., Shapiro, N. M., … others (2014). Seismic velocity changes, strain rate and non-volcanic tremors during the 2009–2010 slow slip event in Guerrero, Mexico. *Geophysical Journal International*, *196*(1), 447–460.

Roux, P., & Ben-Zion, Y. (2014). Monitoring fault zone environments with correlations of earthquake waveforms. *Geophysical Journal International*, *196*(2), 1073–1081.

Sánchez-Pastor, P., Obermann, A., & Schimmel, M. (2018). Detecting and locating precursory signals during the 2011 El Hierro, Canary Islands, submarine eruption. *Geophysical Research Letters*, *45*(19), 10–288.

Sato, H. (1993). Energy transportation in one-and two-dimensional scattering media: analytic solutions of the multiple isotropic scattering model. *Geophysical Journal International*, *112*(1), 141–146.

Schaff, D. P., & Beroza, G. C. (2004). Coseismic and postseismic velocity changes measured by repeating earthquakes. *Journal of Geophysical Research: Solid Earth*, *109*(B10).

Sens-Schönfelder, C., Bataille, K., & Bianchi, M. (2020). High frequency (6 hz) pkpab precursors and their sensitivity to deep earth heterogeneity. *Geophysical Research Letters*, e2020GL089203.

Sens-Schönfelder, C., & Wegler, U. (2006). Passive image interferometry and seasonal variations of seismic velocities at Merapi Volcano, Indonesia. *Geophysical research letters*, *33*(21).

Shearer, P. M., & Earle, P. S. (2004). The global short-period wavefield modelled with a Monte Carlo seismic phonon method. *Geophysical Journal International*, *158*(3), 1103–1117.

Snieder, R., Duran, A., & Obermann, A. (2019). Locating velocity changes in elastic media with coda wave interferometry. *Seismic Ambient Noise*, 188.

Snieder, R., Grêt, A., Douma, H., & Scales, J. (2002). Coda wave interferometry for estimating nonlinear behavior in seismic velocity. *Science*, *295*(5563), 2253–2255.

Takeuchi, N. (2016). Differential monte carlo method for computing seismogram envelopes and their partial derivatives. *Journal of Geophysical Research: Solid Earth*, *121*(5), 3428–3444.

van Dinther, C., Margerin, L., & Campillo, M. (2020). Laterally varying scattering properties in the North Anatolian Fault Zone from ambient noise cross-correlations. *Geophysical Journal International*.

Wegler, U., & Lühr, B. G. (2001). Scattering behaviour at merapi volcano (java) revealed from an active seismic experiment. *Geophysical Journal International*, *145*(3), 579–592.

Wilson, B. C., & Adam, G. (1983). A Monte Carlo model for the absorption and flux distributions of light in tissue. *Medical physics*, *10*(6), 824–830.

Wu, C., Peng, Z., & Ben-Zion, Y. (2009). Non-linearity and temporal changes of fault zone site response associated with strong ground motion. *Geophysical Journal International*, *176*(1), 265–278.

Yamamoto, M., & Sato, H. (2010). Multiple scattering and mode conversion revealed by an active seismic experiment at asama volcano, japan. *Journal of Geophysical Research: Solid Earth*, *115*(B7).

Yoshimoto, K., Wegler, U., & Korn, M. (2006). A volcanic front as a boundary of seismic-attenuation structures in northeastern Honshu, Japan. *Bulletin of the Seismological Society of America*, *96*(2), 637–646.

Zhang, T., Sens-Schönfelder, C., & Margerin, L. (2021). Sensitivity kernels for static and dynamic tomography of scattering and absorbing media with elastic waves: a probabilistic approach. *Geophysical Journal International*.

Supporting Information for: "Implications of laterally varying scattering properties for subsurface monitoring with coda wave sensitivity kernels: application to volcanic and fault zone setting"

Chantal van Dinther [1], Ludovic Margerin [2], Michel Campillo [1]

[1]Université Grenoble Alpes, ISTerre, C.N.R.S., B.P. 53, 38041 Grenoble, France.

[2]Institut de Recherche en Astrophysique et Planétologie, Université Toulouse III Paul Sabatier, C.N.R.S., C.N.E.S, 14, Av. Edouard Belin, 31400 Toulouse, France.

Contents of this file

N/A

Additional Supporting Information (Files uploaded separately)

1. Captions for Movies S1 to S6

Introduction As supporting information, we provide a total of six movies in which the travel-time, decorrelation and scattering sensitivity kernels are shown with increasing lapse-time for a volcanic (S1-S3) and fault zone setting (S4-S6).

Movie S1. Travel-time sensitivity kernel, K_{tt}, for volcanic setting. The volcano is depicted as a circle with radius 6 km and a scattering mean free path $\ell_v = 2$ km, outside the volcano $\ell = 150$ km. The source-detector distance is approximately 47 km. The kernels are normalised with respect to the maximum value.

Movie S2. Decorrelation sensitivity kernel, K_{dc}, for volcanic setting. The volcano is depicted as a circle with radius 6 km and a scattering mean free path $\ell_v = 2$ km, outside the volcano $\ell = 150$ km. The source-detector distance is approximately 47 km. The kernels are normalised with respect to the maximum value.

Movie S3. Scattering sensitivity kernel, K_{sc}, for volcanic setting. The volcano is depicted as a circle with radius 6 km and a scattering mean free path $\ell_v = 2$ km, outside the volcano $\ell = 150$ km. The source-detector distance is approximately 47 km. The kernels are normalised with respect to the maximum value. The color bar is symmetric around 0.

Movie S4. Travel-time sensitivity kernel for fault zone setting with both sources on one side of the fault (dashed lines). The width of the fault zone is 6.25 km. The scattering mean free path in and outside the fault zone are $\ell_{FZ} = 10$ km and $\ell = 150$ km, respectively. The distance between the two sources is approximately 93 km. All kernels are normalised with respect to the maximum value.

Movie S5. Scattering sensitivity kernel for fault zone setting with both sources on one side of the fault (dashed lines). The width of the fault zone is 6.25 km. The scattering mean free path in and outside the fault zone are $\ell_{FZ} = 10$ km and $\ell = 150$ km, respectively.

The distance between the two sources is approximately 93 km. All kernels are normalised with respect to the maximum value. The color bar is symmetric around 0.

Movie S6. Decorrelation sensitivity kernel for fault zone setting with both sources on one side of the fault (dashed lines). The width of the fault zone is 6.25 km. The scattering mean free path in and outside the fault zone are $\ell_{FZ} = 10$ km and $\ell = 150$ km, respectively. The distance between the two sources is approximately 93 km. All kernels are normalised with respect to the maximum value.